Design and Analysis of Consequent-Pole Permanent Magnet Vernier Motor With Cancellation of Even-Order Harmonics

Min-Fu Hsieh[1], Chia-Yuan Chang[1], Thanh-Anh Huynh[1], and D. G. Dorrell[2], *Fellow, IEEE*

[1]Department of Electrical Engineering, National Cheng Kung University, Tainan 701, Taiwan
[2]School of Electrical and Information Engineering, University of the Witwatersrand, Johannesburg 2000, South Africa

This article develops a method for the cancellation of the inherent even-order harmonics in consequent-pole permanent-magnet vernier motors (CP-PMVMs) to improve the performance. Vernier motors can achieve high torque density; however, their high pole number means a high amount of rare-earth permanent magnet (PM) usage at a high cost. The consequent-pole design can reduce PM material cost but leads to high even-order harmonics and torque ripple. This article analyzes two winding configurations in order to develop the method for even-order harmonics cancellation in the CP-PMVMs. Two CP-PMVMs with different slot–pole combinations are analyzed to verify the proposed method. The effect of magnetic barriers on the torque output of the CP-PMVM with canceled even-order harmonics is evaluated. Finally, a multi-objective genetic algorithm is used to optimize the motor. Finite element analysis (FEA) is used to validate the design, with subsequent confirmation of simulations through prototype testing.

Index Terms— **Consequent pole, electric vehicle (EV), even-order harmonic, green transportation, optimization, vernier motor.**

I. Introduction

THE transportation industry has been exploring alternatives to conventional internal combustion engines. Electric vehicles (EVs) are now popular as they can achieve zero emissions on the road [1]. Permanent magnet (PM) motors are the main drive motor choice for EVs due to their high efficiency, high power density, and wide constant power speed range (CPSR) [2]. The conventional approach of coupling these motors with gearboxes or transmissions leads to increased noise, reduced efficiency, and maintenance requirements. Vernier motors, which offer a contactless magnetic gearing effect, may provide a solution to the gearbox issue. They have the potential to enhance system efficiency and reduce noise levels, thus offering a better driving experience for EV users [3], [4].

PM vernier motors (PMVMs) have high torque density and simple structure. Several studies have investigated the effect of flux leakage and slot opening on surface-mounted PMVMs (SPMVMs) and proposed analytical approaches to optimize their performance [5], [6], [7]. For instance, a high torque density direct-drive SPMVM was designed for automated guided vehicle applications [5]. However, commercialization of PMVMs still faces challenges, mainly due to their high cost of PM and low power factor [8], [9]. To address these issues, various techniques have been proposed to improve their power factor, including the use of dual stators [10], Halbach arrays [11], and dc field windings [12].

To reduce the amount of PM used in PMVMs, a consequent pole design can be an effective option. These involve replacing either the PM N or S poles with iron cores, which reduces the amount of PM needed. Additionally, this design can strengthen the rotor structure by embedding the PMs on the rotor surface. Studies have shown that this design can maintain or even enhance the electromagnetic performance of the original motor while reducing PM usage [13]. For example, the power factor of a consequent-pole PMVM (CP-PMVM) was enhanced, and the output torque maintained in comparison to conventional PMVMs in [14] and [15]. However, in the CP-PMVMs, both odd-order and even-order harmonics appear, which causes torque ripple and diminishes performance. Therefore, eliminating even-order harmonics is key to this problem.

In this article, a mathematical model is first derived for CP-PMVMs. Two different winding configurations are compared, and a method is developed for the cancellation of even-order harmonics. Flux barriers are used to concentrate flux, and the size of the flux barriers is determined, so that motor performance is improved. By using a response surface methodology (RSM) with a multi-objective genetic algorithm (MOGA) for optimization, the motor performance is further improved, PM usage is reduced, and the motor is designed to operate without even-order harmonics. To validate the derivation and design, finite element analysis (FEA) is conducted, and a prototype is tested.

II. Even-Order Harmonics Cancellation of CP-PMVM

A. Even-Order Harmonics

The PMVM possesses a magnetic gearing effect, which couples the stator and rotor magnetic fields over certain harmonic orders, so that a higher air-gap magnetic flux density can be achieved compared to a conventional surface or interior PM motor. The characteristics that produce magnetic gearing effect can be expressed as [16]

$$P_r = N_s \pm P_s \tag{1}$$

where P_s is the number of stator pole pairs, N_s is the stator tooth number, and P_r is the rotor pole-pair number. Note that the three-phase current sequence for a vernier motor is

Manuscript received 28 March 2023; revised 11 June 2023; accepted 4 July 2023. Date of publication 7 July 2023; date of current version 24 October 2023. Corresponding author: M.-F. Hsieh (e-mail: mfhsieh@mail.ncku.edu.tw).

Color versions of one or more figures in this article are available at https://doi.org/10.1109/TMAG.2023.3293268.

Digital Object Identifier 10.1109/TMAG.2023.3293268

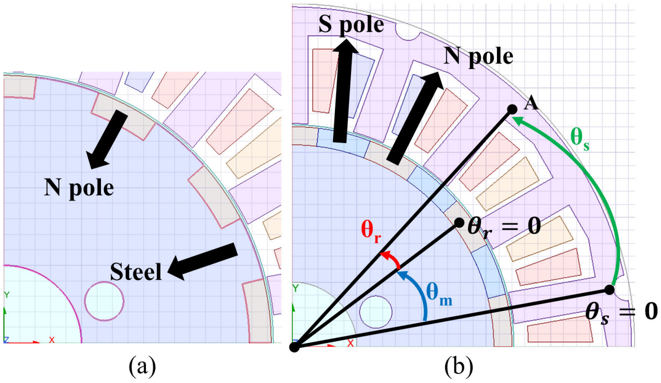

Fig. 1. (a) Consequent pole PMVM. (b) Conventional PMVM.

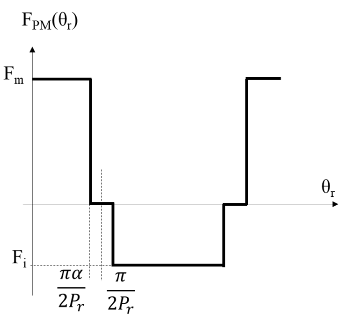

Fig. 2. MMF waveform of CP-PMVM.

negative when $P_r = N_s - P_s$. This means that the dominant rotating mangetic fields of the rotor and the stator can be synchronized when the speed and frequency are correct.

The consequent pole replaces the PM N or S poles of with iron poles, as shown in Fig. 1(a). Using consequent poles can reduce flux leakage and possibly enhance torque output. In Fig. 1(b), θ_r is rotor position referring to a specific PM center; θ_s is stator position referring to peak current position of Phase A, as indicated; θ_m is defined as $\theta_s - \theta_r$.

The MMF waveform of the CP-PMVM, F_{cp}, is shown in Fig. 2, which is expressed in the form of a Fourier series [13]

$$F_{\text{cp}}(\theta_s, t) = F_0 + \sum_{n=1}^{\infty} F_n \cos(nP_r\theta_s - nP_r\Omega_r t) \tag{2}$$

where

$$F_0 = \frac{\alpha}{2}F_m - \left(1 - \frac{w_s}{2}\right)F_i \tag{3}$$

$$F_n = \frac{2}{n\pi}\left[F_m \sin\left(\frac{n\alpha\pi}{2}\right) + F_i \sin\left(\frac{nw_s\pi}{2}\right)\right] \tag{4}$$

where F_m is an N pole equivalent MMF, F_i is the equivalent iron pole MMF, Ω_r is the rotor electrical angular velocity, w_s is the ratio of the distance between the magnet and the steel to the length of a pole pair, and α is the flux concentration factor. Note that the S-pole PM is replaced in this case.

Equations (2)–(4) show that the MMF waveform contains both odd- and even-order harmonics, which would affect the flux density distributions and back electromotive force (back EMF) waveforms. The back EMF can be calculated

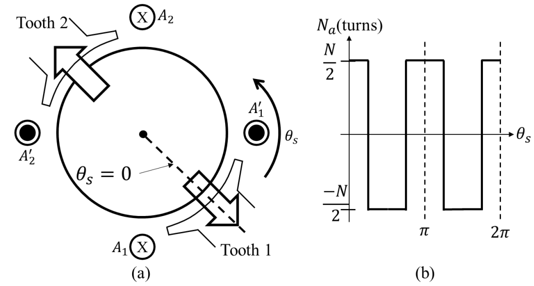

Fig. 3. (a) First winding configuration. (b) Winding function [17].

using

$$e_a(\theta_s, t) = -\frac{d\varphi_a}{dt} = -\frac{d}{dt}\int_0^{2\pi} gl_{st}B_{\text{cp}}(\theta_s, t)N_a(\theta_s)d\theta_s \tag{5}$$

where g is the air-gap length, $B_{\text{cp}}(\theta_s, t)$ is the flux density, which is calculated by multiplying the MMF in (2) and air-gap permeability, φ_a is the single-phase flux, l_{st} is the rotor stack length, and $N_a(\theta_s)$ is the single-phase winding function.

B. Even-Order Harmonics Cancellation

As can be seen in (5), it is possible to reduce the even-order harmonics of the back EMF by manipulating the winding layout (N_a). Two different winding configurations are considered. Fig. 3 shows the first condition of the winding configuration in the CP-PMVM, where the arrows indicating the winding directions are both outward [17]. Note that the winding (arrow) directions are derived from the right-hand rule.

In Fig. 3, the winding function can be expressed as

$$\begin{cases} \frac{N}{2}, & 0 \le \theta_s \le \frac{\pi}{4} \\ -\frac{N}{2}, & \frac{\pi}{4} \le \theta_s \le \frac{3\pi}{4} \\ \frac{N}{2}, & \frac{3\pi}{4} \le \theta_s \le \frac{5\pi}{4} \\ -\frac{N}{2}, & \frac{5\pi}{4} \le \theta_s \le \frac{7\pi}{4} \\ \frac{N}{2}, & \frac{7\pi}{4} \le \theta_s \le 2\pi \end{cases} \tag{6}$$

where N is the number of turns.

Fig. 4 shows the second winding condition, where one arrow is inward and the other outward. The winding function can thus be expressed as [18]

$$\begin{cases} \frac{N}{2}, & 0 \le \theta_s \le \frac{\pi}{4} \\ 0, & \frac{\pi}{4} \le \theta_s \le \frac{3\pi}{4} \\ -\frac{N}{2}, & \frac{3\pi}{4} \le \theta_s \le \frac{5\pi}{4} \\ 0, & \frac{5\pi}{4} \le \theta_s \le \frac{7\pi}{4} \\ \frac{N}{2}, & \frac{7\pi}{4} \le \theta_s \le 2\pi. \end{cases} \tag{7}$$

Based on the above two winding configurations, the fundamental and second-order harmonic waveforms of air-gap flux density in the same period are presented in Figs. 5 and 6. The blue waveform in the upper part of Fig. 5 represents the fundamental wave of air-gap flux density, while the red one shows the second-order harmonic, where the stator teeth and winding direction are indicated. In each winding condition,

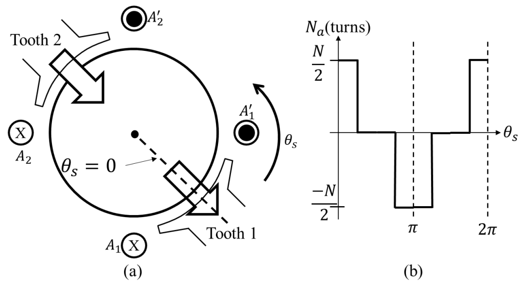

Fig. 4. (a) Second winding condition. (b) Winding function [18].

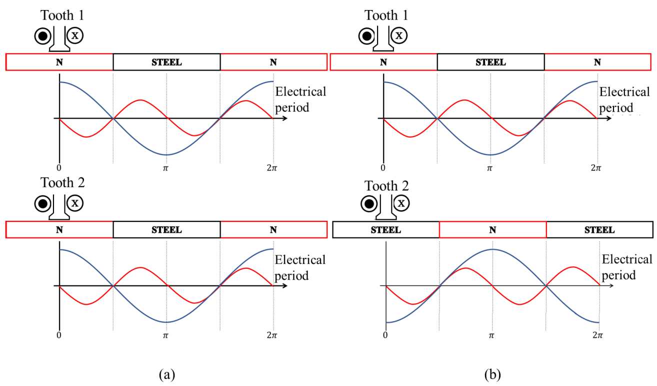

Fig. 5. Fundamental and second-order harmonics. (a) Winding one with scenario 1. (b) Winding one with scenario 2.

two possible scenarios exist for the teeth wound by the single-phase winding. In the first scenario [Fig. 5(a)], all teeth and windings align with the same pole, allowing for the superposition of fundamental waves but not eliminating even-order harmonics. In the second scenario [Fig. 5(b)], the fundamental waves are canceled, but even-order harmonics are added. Note that these two scenarios are caused by different pole–slot combinations. For the second winding and first scenario in Fig. 6(a), both fundamental and even-order harmonics are canceled. In the second scenario in Fig. 6(b), the fundamental waves are added and even-order harmonics are canceled. These are summarized in Table I.

From the previous discussion, it can be concluded that two conditions should be simultaneously satisfied to eliminate second-order harmonics.

1) The winding directions of the coils in one phase should be half outward and half inward.
2) Those outward should face different rotor poles from that of the inward at any moment; for example, all those outward facing N while the inward S (iron pole).

Table II summarizes some examples (gear ratios 1–3) whose pole–slot combinations can meet the condition of winding layout 2, scenario 2 to cancel even-order harmonics. Note that only concentrated windings are considered for a compact design required by electric scooters.

III. Analytical Models and Simulations

To verify the principle of even-order harmonic cancellation, two test 3 kW CP-SPMVM models: Models 1 and 2, are

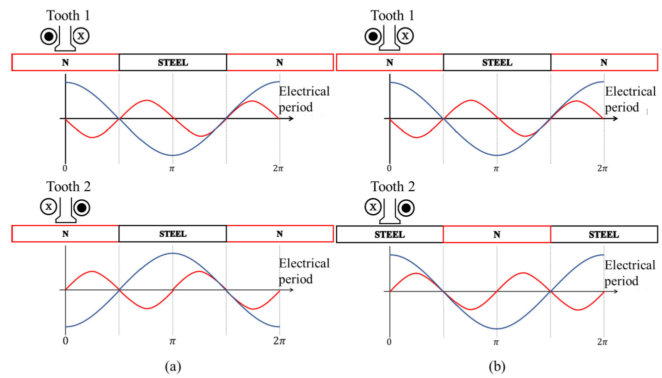

Fig. 6. Fundamental and second-order harmonics. (a) Winding two with scenario 1. (b) Winding two with scenario 2.

TABLE I
Even-Order Harmonics and Windings

Back EMF		Fundamentals	2nd-order Harm.
Winding layout #1	scenario 1	added	added
	scenario 2	canceled	added
Winding layout #2	scenario 1	canceled	canceled
	scenario 2	added	canceled

TABLE II
Pole–Slot Combination to Eliminate Even-Order Harmonics

Stator pole pairs	Teeth number	Gear ratio
5	12	1.4
5	18	2.6
7	18	1.57
7	24	2.42
11	24	1.18
9	30	2.33
11	30	1.72
13	30	1.3

considered, as shown in Fig. 7. The slot–pole combinations are 18 s/12 p and 18 s/13 p, respectively, causing the gear ratios (G_r) to be 2 and 2.6, respectively. Model 1 represents the first winding configuration, while Model 2 indicates the second.

A. Air-Gap Flux Density and Back EMF Comparison

The FEA simulation is carried out using Ansys Maxwell. Table III shows that the even-order (second and fourth) back EMF harmonics for the case where $G_r = 2.6$ is eliminated (but not for that of $G_r = 2$), as can be observed in Fig. 8.

B. Effect of Magnetic Barriers on Torque

The difference of permeability between the steel pole and PM results in an asymmetrical air-gap flux density. Therefore, the flux density of the iron poles is higher than that of the PM. This further causes saturation of the stator teeth and part of the rotor iron poles, as shown in Fig. 9(a). This can be mitigated by arranging barriers at both ends of each PM, which is designed using two geometrical parameters: length (L_{m1}) and span (α),

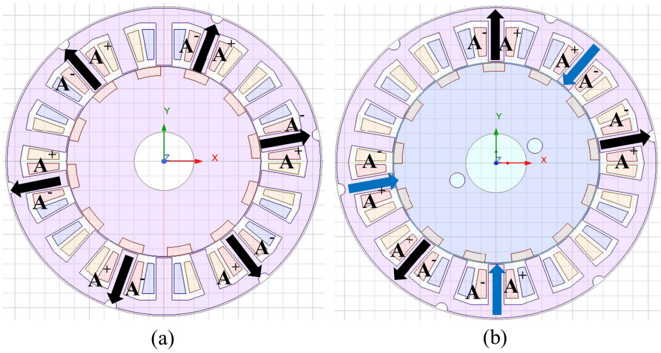

Fig. 7. (a) Model 1 with Gr = 2 and winding layouts. (b) Model 2 with Gr = 2.6 and winding layouts.

TABLE III
COMPARISON OF BACK EMF HARMONICS

Harmonic order	$G_r = 2$ Back EMF harmonic amplitude	$G_r = 2.6$ Back EMF harmonic amplitude
1	12.58	12.68
2	0.84	0
3	0.034	0.28
4	0.38	0
5	0.65	0.17
THD (%)	8.9	2.5

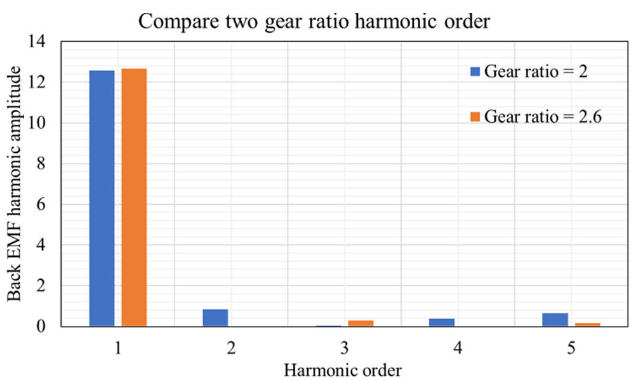

Fig. 8. Harmonic orders of PMVMs with gear ratios 2 and 2.6.

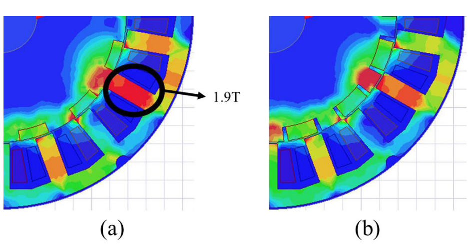

Fig. 9. (a) Without barriers flux density. (b) With barriers flux density.

as indicated in Fig. 10. The case when $G_r = 2.6$ is simulated since there is no even-order harmonic.

Regulating the size of the barriers can modify the reluctance and the flux direction. The results in Fig. 10 show that when α or L_{m1} is small, leakage flux is significant, resulting in lower torque. In contrast, when L_{m1} or α is too large, leakage flux may be reduced; however, the flux is concentrated on the narrower rotor steel poles, resulting in saturation. Appropriate barrier sizes at both ends of the PM can effectively reduce leakage, enhance the performance, and improve saturation [as illustrated in Fig. 9(b)].

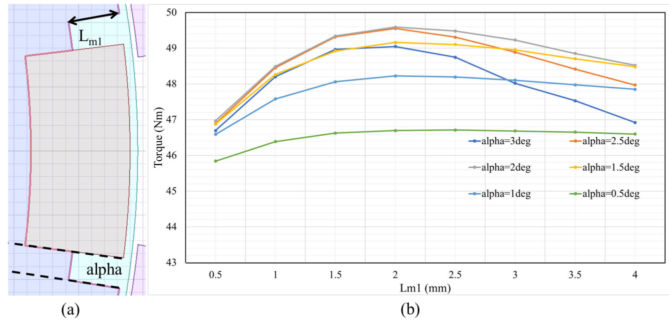

Fig. 10. (a) Barrier parameter. (b) Torque variations.

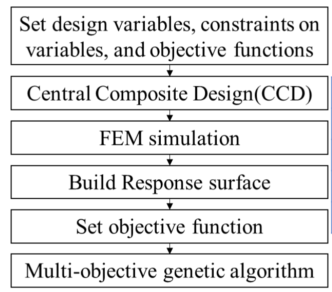

Objective
Maximum torque > 48 N-m
Current density ≤ 20 A/mm²
Line voltage ≤ 43 V_{max}
390 mm²≤ magnet usage ≤ 400 mm²

(a) (b)

Fig. 11. (a) Optimization process. (b) Objectives.

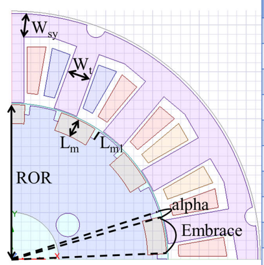

Change parameter	
	Scope
Teeth (mm)	4.5 ~ 6
Yoke (mm)	4.5 ~ 6.5
Rotor diameter (mm)	62 ~ 70
Magnet thickness (mm)	3 ~ 4.5
Cϕ = embrace	0.9 ~ 1.1
Alpha (o)	0.5 ~ 2.5
Lm1 (mm)	0.5 ~ 4
Current advanced angle (o)	10 ~ 15
Turns	4 、5、6

(a) (b)

Fig. 12. (a) Motor parameters. (b) Parameter variation range.

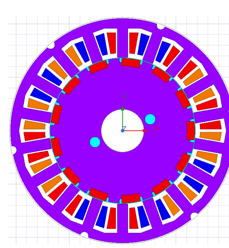

	Before opti.	after opti.
Teeth (mm)	5	5.0283
Yoke (mm)	5	4.5181
Rotor diameter (mm)	69	67.695
Magnet thickness (mm)	3.85	3.5669
Cϕ = embrace	1	1.0806
Alpha (o)	2	1.9491
Lm1 (mm)	2	1.8206
Current advanced angle (o)	12	14.111
Turns	5	5

(a) (b)

Fig. 13. (a) Optimized PMVM. (b) Parameters before and after optimization.

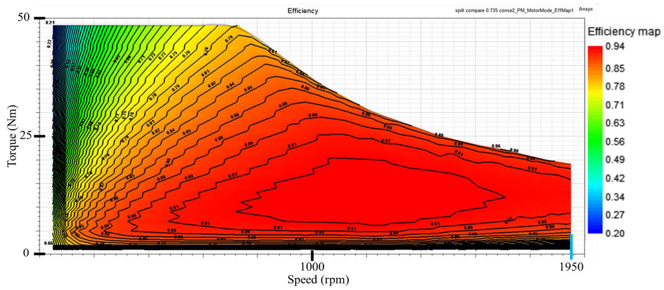

Fig. 14. Efficiency map (3 kW, max speed 1950 r/min, max torque 48 N-m at 650 r/min, and max efficiency 93.6%).

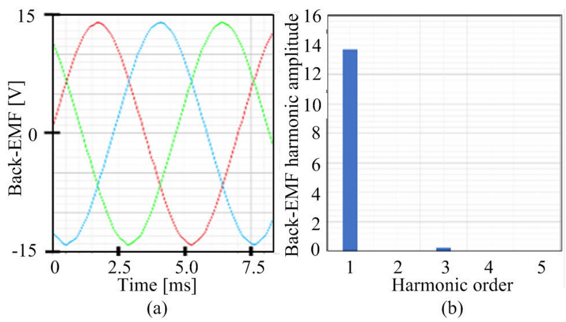

Fig. 15. (a) Back EMF waveform. (b) Harmonic order after optimization.

C. Design Optimization

The RSM with a MOGA is used to optimize a CP-PMVM applied to electric scooters (requiring 48 N-m at 650 r/min and 18 N-m at 1950 r/min, both at 43.2 V). The optimization process and objectives are shown in Fig. 11. First, the central composite design (CCD) is used in the design of experiments (DOEs) approach to obtain the sample nine design variables shown in Fig. 12. These variables are used for the FEA simulation, whose results are used to build a response surface. Finally, the MOGA is used to obtain an optimized design.

The optimized CP-PMVM and its parameters before and after optimization are shown in Fig. 13. The motor efficiency map is shown in Fig. 14, where it can be seen that the maximum torque is 48.5 N-m, maximum efficiency is 93.6%, and torque density is 62 kN-m/L. The base speed at the maximum torque at 180 A is 650 r/min, and the speed achieves 1950 r/min. The back EMF waveform and its harmonic order are shown in Fig. 15, where the even harmonics are eliminated.

IV. Measurements

The designed vernier motor $G_r = 2.6$ was prototyped, as shown in Fig. 16.

The prototype was first tested at no load. The measured phase back EMF at 650 r/min is shown in Fig. 17, where the peak-to-peak value is 26.17 V. Compared with the simulation value of 26.58 V (waveforms not shown), the error percentage is 1.54%, which validates the design. Moreover, there is little even-order harmonics in the waveform.

The gear ratio G_r and rotor speed N_r relationship is given as

$$f_e = \frac{G_r N_r P_s}{60} \tag{8}$$

where f_e is the electric frequency of the motor.

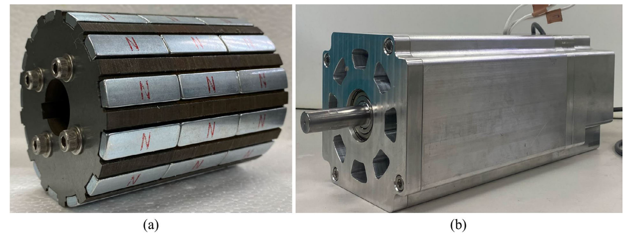

Fig. 16. (a) Rotor without shaft. (b) Motor.

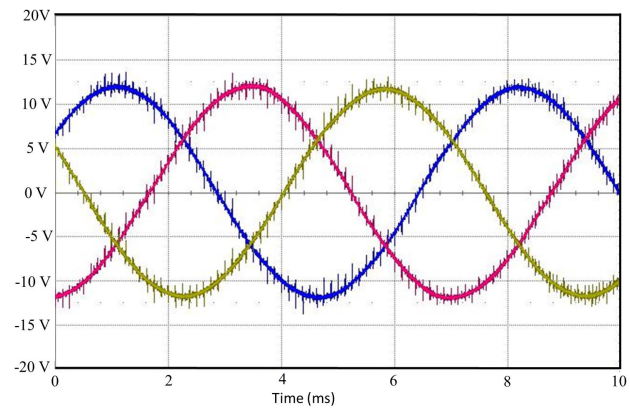

Fig. 17. Measured back EMF waveform at 650 r/min.

TABLE IV
Gear Ratio Verification

Performance term	value
Speed (rpm)	650
Theoretical frequency (Hz)	140.83
Test frequency (Hz)	140.65
Error (%)	0.12

TABLE V
Motor Performance Comparison

Item	Simulation	Simulation after modification	Experiment
Speed (rpm)	650		
Current (A_{rms})	8.2	9	10.17
Torque (N-m)	3.47	3.52	3.52
Efficiency (%)	87.5	85.5	83.75

From (8), a comparison between the theoretical and measured frequencies is given in Table IV. As can be seen, both cases agree well.

The motor performance at light load at 650 r/min was measured (considering the limitation of the test bench and inverter). Table V shows the comparison of output torque and efficiency between the simulation and measurements. Note that due to manufacturing issues, the conductors used in the prototype were reduced from 1.1 mm six strands to 1.1 mm two strands with a much lower slot fill factor. Consequently, the phase resistance increases from 21 to 62 mΩ. This increases the resistance significantly and affects the motor efficiency and torque. Simulations were further conducted using the prototype parameters, and as can be observed in Table V, the results match the measurements well. This validates the simulations.

V. Conclusion

This article has developed a method to cancel the inherent even-order harmonics in the CP-PMVM for EV applications. The two necessary conditions for achieving this target have been discussed and summarized. The PM usage for the general vernier motor (without consequent poles and same designs) at gear ratio 2.6 is 516.17 mm^2. After optimizing the vernier motor with consequent poles, the PM usage is 396.79 mm^2, which is a reduction of 23%. Two CP-PMVMs have been used to demonstrate the effect of even-order harmonic cancellation, which was validated using FEA. Optimization was conducted to enhance the motor performance. The measurement on the prototyped PMVM validates the simulation accuracy.

Acknowledgment

ANSYS Inc. is acknowledged for supporting ANSYS/ Maxwell software.

References

[1] R. Vazquez-Duhalt, "Environmental impact of used motor oil," *Sci. Total Environ.*, vol. 79, no. 1, pp. 1–23, Feb. 1989.

[2] H. Wang and J. Leng, "Summary on development of permanent magnet synchronous motor," in *Proc. Chin. Control Decis. Conf. (CCDC)*, Jun. 2018, pp. 689–693.

[3] O. Barth, "Harmonic piezodrive—Miniaturized servo motor," *Mechatronics*, vol. 10, nos. 4–5, pp. 545–554, Jun. 2000.

[4] A. Toba and T. A. Lipo, "Novel dual-excitation permanent magnet Vernier machine," in *Proc. 34th IEEE Ind. Appl. Conf. IAS Annu. Meeting*, Oct. 1999, pp. 2539–2544.

[5] Y. Shi and T. W. Ching, "Power factor analysis of dual-stator permanent magnet Vernier motor with consideration on turn-number assignment of inner and outer stator windings," *IEEE Trans. Magn.*, vol. 57, no. 2, pp. 1–5, Feb. 2021.

[6] J. Zhu, Y. Zuo, H. Chen, J. Chen, and C. H. T. Lee, "Deep-investigated analytical modeling of a surface permanent magnet Vernier motor," *IEEE Trans. Ind. Electron.*, vol. 69, no. 12, pp. 12336–12347, Dec. 2022.

[7] J. Zhu, Y. Fan, H. Chen, J. Chen, Y. Zuo, and C. H. T. Lee, "Comprehensive armature reaction modeling and flux weakening optimization of a surface permanent magnet Vernier motor," *IEEE Trans. Ind. Electron.*, vol. 70, no. 9, pp. 8709–8722, Sep. 2023.

[8] F. Wu and A. M. EL-Refaie, "Permanent magnet Vernier machines: A review," in *Proc. 13th Int. Conf. Electr. Mach. (ICEM)*, Sep. 2018, pp. 372–378.

[9] D. Li, R. Qu, and T. Lipo, "High power factor Vernier permanent magnet machines," in *Proc. IEEE Energy Convers. Congr. Expo.*, Sep. 2013, pp. 1534–1540.

[10] N. Baloch, B. Kwon, and Y. Gao, "Low-cost high-torque-density dual-stator consequent-pole permanent magnet Vernier machine," *IEEE Trans. Magn.*, vol. 54, no. 11, pp. 1–5, Nov. 2018.

[11] Y. Kataoka, M. Takayama, Y. Matsushima, and Y. Anazawa, "Design of surface permanent magnet-type Vernier motor using Halbach array magnet," in *Proc. 18th Int. Conf. Electr. Mach. Syst. (ICEMS)*, Oct. 2015, pp. 177–183.

[12] T. W. Ching, K. T. Chau, and W. Li, "Power factor improvement of a linear Vernier permanent-magnet machine using auxiliary DC field excitation," *IEEE Trans. Magn.*, vol. 52, no. 7, pp. 1–4, Jul. 2016.

[13] Z. Chen, J. Wang, and L. Zhou, "Design and analysis of permanent magnet Vernier motors for downhole applications," in *Proc. 1st IEEE China Int. Youth Conf. Electr. Eng. (CIYCEE)*, Nov. 2020, pp. 1–6.

[14] Z. Chen, J. Wang, Z. Hu, J. Xiao, L. Zhou, and H. Wang, "Design of consequent pole permanent magnet Vernier motor for downhole electric drilling system," in *Proc. 4th IEEE Student Conf. Electr. Mach. Syst. (SCEMS)*, Dec. 2021, pp. 1–6.

[15] A. Rehman and B. Kim, "Characteristics analysis of consequent-pole ferrite magnet Vernier machine using novel equivalent magnetic circuit," *IEEE J. Emerg. Sel. Topics Power Electron.*, vol. 10, no. 2, pp. 1823–1833, Apr. 2022.

[16] D. Li, R. Qu, J. Li, and W. Xu, "Consequent-pole toroidal-winding outer-rotor Vernier permanent-magnet machines," *IEEE Trans. Ind. Appl.*, vol. 51, no. 6, pp. 4470–4481, Nov./Dec. 2015.

[17] G. Joksimović, "A.C. Winding analysis using a winding function approach," *Int. J. Electr. Eng. Educ.*, vol. 48, no. 1, pp. 34–52, Jan. 2011.

[18] W. Liu and T. A. Lipo, "Analysis of consequent pole spoke type Vernier permanent magnet machine with alternating flux barrier design," *IEEE Trans. Ind. Appl.*, vol. 54, no. 6, pp. 5918–5929, Nov./Dec. 2018.